Full length article

Regional biomechanical characterization of human ascending aortic aneurysms: Microstructure and biaxial mechanical response

Federica Cosentino [a,b], Selda Sherifova [c], Gerhard Sommer [c], Giuseppe Raffa [d], Michele Pilato [d], Salvatore Pasta [b,d], Gerhard A. Holzapfel [c,e,*]

[a] *Ri.MED Foundation, Palermo, Italy*
[b] *Department of Engineering, University of Palermo, Italy*
[c] *Institute of Biomechanics, Graz University of Technology, Austria*
[d] *Department for the Treatment and Study of Cardiothoracic Diseases and Cardiothoracic Transplantation, IRCCS-ISMETT, Palermo, Italy*
[e] *Department of Structural Engineering, Norwegian Institute of Science and Technology (NTNU), Trondheim, Norway*

ARTICLE INFO

ABSTRACT

The ascending thoracic aortic aneurysm (ATAA) is a permanent dilatation of the vessel with a high risk of adverse events, and shows heterogeneous properties. To investigate regional differences in the biomechanical properties of ATAAs, tissue samples were collected from 10 patients with tricuspid aortic valve phenotype and specimens from minor, anterior, major, and posterior regions were subjected to multi-ratio planar biaxial extension tests and second-harmonic generation (SHG) imaging. Using the data, parameters of a microstructure-motivated constitutive model were obtained considering fiber dispersion. SHG imaging showed disruptions in the organization of the layers. Structural and material parameters did not differ significantly between regions. The non-symmetric fiber dispersion model proposed by Holzapfel et al. [25] was used to fit the data. The mean angle of collagen fibers was negatively correlated between minor and anterior regions, and the parameter associated with collagen fiber stiffness was positively correlated between minor and major regions. Furthermore, correlations were found between the stiffness of the ground matrix and the mean fiber angle, and between the parameter associated with the collagen fiber stiffness and the out-of-plane dispersion parameter in the posterior and minor regions, respectively. The experimental data collected in this study contribute to the biomechanical data available in the literature on human ATAAs. Region-specific parameters for the constitutive models are fundamental to improve the current risk stratification strategies, which are mainly based on aortic size. Such investigations can facilitate the development of more advanced finite element models capable of capturing the regional heterogeneity of pathological tissues.

Statement of Significance

Tissue samples of human ascending thoracic aortic aneurysms (ATAA) were collected. Samples from four regions underwent multi-ratio planar biaxial extension tests and second-harmonic generation imaging. Region-specific parameters of a microstructure-motivated model considering fiber dispersion were obtained. Structural and material parameters did not differ significantly between regions, however, the mean fiber angle was negatively correlated between minor and anterior regions, and the parameter associated with collagen fiber stiffness was positively correlated between minor and major regions. Furthermore, correlations were found between the stiffness of the ground matrix and the mean fiber angle, and between the parameter associated with the collagen fiber stiffness and the out-of-plane dispersion parameter in the posterior and minor regions, respectively. This study provides a unique set of mechanical and structural data, supporting the microstructural influence on the tissue response. It may facilitate the development of better finite element models capable of capturing the regional tissue heterogeneity.

* Corresponding author at: Institute of Biomechanics, Graz University of Technology, Austria.
E-mail address: holzapfel@tugraz.at (G.A. Holzapfel).

1. Introduction

Ascending thoracic aortic aneurysms (ATAAs) are characterized by abnormal dilation of the ascending aorta, with the vessel diameter exceeding the normal values of 2–3 cm [1]. Although it is a relatively rare event, with an estimated incidence of 5/100 000 individuals per year [2,3], the risk of fatal complications such as aortic rupture or acute dissection can be as high as 50% in patients with a diameter larger than 50 mm [4], mainly in men between 50 and 70 years [5]. Current diagnosis and risk assessment are primarily based on maximum aortic diameter [6–8], although aortic size can be normalized by body mass index for greater sensitivity and accuracy [9].

Elective surgery is typically recommended when the aortic diameter exceeds 5.0 cm in women or 5.5 cm in men [6,10] or if the maximal diameter in an aorta increases more than 0.5 to 1.0 cm in one year [11,12], since the annual risk of dissection or rupture increases from 3% to 7% with aneurysms larger than 6 cm in diameter [7]. Because the risk of adverse events in ATAA is typically assessed only by diagnostic imaging, clinical decision-making does not include the mechanical and structural changes that are likely to occur with the development and progression of aneurysms [13–16]. As a result, the current approach based on the aortic size is considered a poor prognostic parameter [17]. Vorp et al. [14] reported a 5-year mortality rate of 39% for ATAAs below the 6 cm diameter threshold and 62% for ATAAs above the 6 cm diameter threshold, reflecting the inefficiency of the diameter criterion.

Studies on arteries indicate that the mechanical environment and biomechanical factors of arteries play important roles in the onset and progression of cardiovascular diseases such as ATAA. Therefore, biomechanically based criteria represent a promising approach to evaluate and predict the course of aortic diseases, and a better understanding of the mechanical behavior of aneurysms is fundamental to improve the clinical decision-making strategies and to design implants and artificial tissue equivalents. There is growing interest in developing strategies to estimate the risk of ATAA rupture based on the contribution of both ATAA biomechanics, i.e. hemodynamic and intramural stress and molecular biomarkers to improve clinical outcomes [18–20].

It is known that the collagen fiber organization determines the mechanical behavior of soft fibrous tissues, particularly through their orientation and dispersion [21–26]. However, regional differences in the organization and mechanics of collagen fibers in ATAA tissues have not been adequately investigated, and this knowledge is invaluable for a better understand of the local mechanobiological processes that control the mechanics of thoracic aortic aneurysms [27]. In this study, we report the regional mechanical and microstructural differences of human ATAAs from patients with tricuspid aortic valves realized using multi-ratio planar biaxial extension tests and second-harmonic generation (SHG) imaging. More specifically, structural parameters of the constitutive model introduced in [25] were obtained from SHG images and mechanical data were used to obtain the material parameters of the model. The structural and material parameters were then compared between the four regions of the aneurysmal ascending aorta.

2. Materials and methods

2.1. Materials

ATAA samples were obtained from 3 female and 7 male patients undergoing elective surgical repair of the aneurysmal ascending aorta because the diameter was larger than the surgical threshold [12]. The human ATAA samples were characterized by the presence of a tricuspid valve, the mean patient age was 74.4 ± 6.8 years (mean$\pm$SD) and ranged from 67 to 88 years. The mean diameter of

Table 1
Demographics of the study population, including age, sex, aneurysm diameter, and thickness of specimens from different regions (see Fig. 1).

Donor	Age	Sex	Diameter [mm]	Thickness [mm]			
				Minor	Anterior	Major	Posterior
ATAA-1	80	F	50	2.2	2.1	2.1	2.25
ATAA-2	68	F	47	2.5	2.8	2.25	2.6
ATAA-3	68	M	43	2.67	2.35	2.5	3.3
ATAA-4	78	M	54	2.7	2.08	2.2	2.3
ATAA-5	88	M	58	–	–	2.1	2.2
ATAA-6	71	M	49	2.12	2.3	2.25	2.15
ATAA-7	67	M	54	2.9	1.96	2.2	3
ATAA-8	78	F	55	2.7	2.08	2.2	2.3
ATAA-9	79	M	56	3	2.66	2.16	1.89
ATAA-10	67	M	54	2.4	1.8	2.26	2.16

the aneurysms measured by echocardiography was 52 ± 4.61 mm and ranged from 43 to 58 mm. Postoperatively, ATAA samples were cryopreserved in calcium- and glucose-free 0.9% physiological saline solution and stored at $-80\,°C$ until mechanical examination. Before performing the biaxial test, the samples were slowly thawed overnight at room temperature.

The aortic ring was cut lengthwise to obtain a flat sheet, see Fig. 1. Square specimens (10×10 mm) were obtained from the minor, anterior, major and posterior curvature to perform biaxial mechanical tests, see Fig. 1(b). The specimen thickness was measured optically with a CCD camera according to Sommer et al. [28].

In addition, rectangular specimens of 7×11 mm were excised from the aortic ring with the longer side lengthwise, see Fig. 1(b), and placed in 4% formaldehyde for at least 12 h for adequate fixation.

Table 1 summarizes clinical demographics and thickness measurements for all specimens obtained from 10 ATAA samples. The study protocol was approved by the local ethical committee of IS-METT IRCCS (IRRB/04/14) and informed consent was obtained for all patients.

2.2. Data acquisition

2.2.1. Multi-photon microscopy

The specimens to be imaged were optically cleared according to the protocol in [29], see Fig. 2. After a brief immersion in phosphate buffered saline (PBS) to get rid of the excess formaldehyde, the specimens were dehydrated by immersion in a graded ethanol series consisting of ethanol solutions at concentrations of 50, 70, twice 95 and 100% each for 30 mins. Next, the specimens were placed in a 1:2 solution of ethanol: benzyl alcohol-benzyl benzoate (BABB) for 4 h, followed by immersion in 100% BABB for at least 12 h. All steps were performed at room temperature.

SHG imaging was performed at the Institute of Molecular Biosciences, University of Graz, Austria. Optically cleared specimens were excited with an 880 nm laser using a Leica TCS SP5 multiphoton microscope equipped with a 25×0.95 water objective with a working distance of 2.5 mm for deep tissue imaging and the SHG signal was collected with a 460/50 band-pass filter. In-plane images (z-stacks) were acquired from the circumferential-longitudinal plane through the specimen thickness where the penetration depth allows, with a sampling of $620 \times 620 \times 5$ µm (image size × step size). If the penetration depth was not sufficient to image the entire thickness of the optically cleared specimen, the specimen was inverted under the microscope and another in-plane image stack was obtained. Out-of-plane images were acquired from the circumferential-radial plane with a sampling of 620×620 µm. All images were acquired with 1024×1024 pixels.
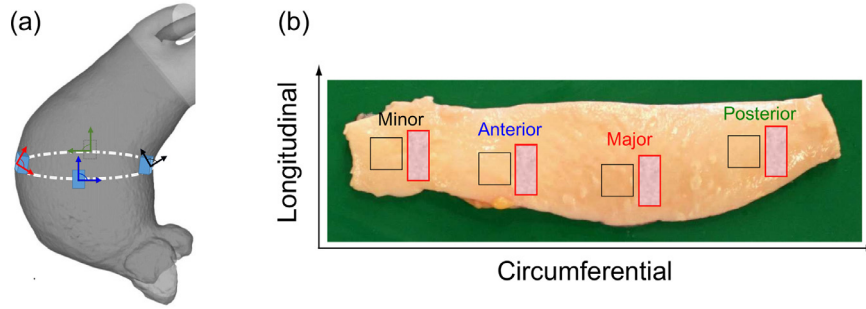
Fig. 1. (a) Schematic illustration of the ascending aortic aneurysm and (b) aortic tissue cleaned and opened with a longitudinal incision showing samples for biaxial extension tests and SHG microscopy indicated with black squares and red rectangles from minor, anterior, major, and posterior regions, respectively.
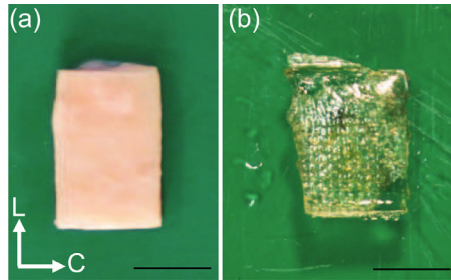

Fig. 2. (a) ATAA-4 specimen for SHG imaging before and (b) after formaldehyde fixation and optical clearing. L and C denote the longitudinal and circumferential directions, respectively. The scale bar indicates 5 mm.

Fig. 3. Unit vector **N** representing an arbitrary fiber direction defined by the angles Θ (elevation angle) and Φ (angle between the $\mathbf{e}_1$ direction and the projection of **N** in the $\mathbf{e}_1 - \mathbf{e}_2$ plane) relative to the rectangular Cartesian unit basis vectors ($\mathbf{e}_1$, $\mathbf{e}_2$, $\mathbf{e}_3$). Adopted from Holzapfel et al. [25].

2.2.2. Biaxial extension testing

After thickness measurement, black powder markers were applied to the specimen to generate a speckle pattern suitable for optical tracking. The specimens were mounted on the device, for device specifications see [30], using three equidistantly placed hooks connected with a string on each side. Next, a stretch-driven protocol was executed quasi-statically at a rate of 2 mm/min starting at 1.05 stretch with a stretch increment of 0.05 to rupture. At each increment, the specimen was first subjected to four preconditioning cycles with a 1:1 loading ratio between longitudinal λ_{long} and circumferential direction λ_{circ}. Then the measurement cycles with different ratios $\lambda_{\text{long}}:\lambda_{\text{circ}} = \{1:1, 1:0.75, 0.75:1, 1:0.5, 0.5:1\}$ were executed. In addition, relaxation tests were conducted with a ramp speed of 100 mm/min and a duration of 15 min at each stretch level following the quasi-static multi-ratio test. Tests were performed in a PBS bath heated and maintained at 37 °C. The forces of the four linear actuators as well as the stretches in circumferential and longitudinal directions were recorded throughout the tests and exported for data analyses.

2.3. Data analyses

2.3.1. Material model

The artery is modeled as a purely elastic, incompressible, and fiber-reinforced material using the strain-energy function described in [25], which sums the contributions of the ground substance and the two symmetrical families of collagen fibers, assuming that the mechanical properties of both families are the same. The total strain energy is given by

$$\Psi = \Psi_{\text{g}}(\mathbf{C}) + \sum_{i=4,6} \Psi_{\text{fi}}(\mathbf{C}, \mathbf{H}_i), \tag{1}$$

where $\mathbf{C} = \mathbf{F}^{\text{T}}\mathbf{F}$ is the right Cauchy-Green tensor with the deformation gradient $\mathbf{F}$, and $\mathbf{H}_i$ are generalized structure tensors that quantify the fiber dispersion. The contributions of the ground matrix and the collagen fiber family to the strain-energy function in
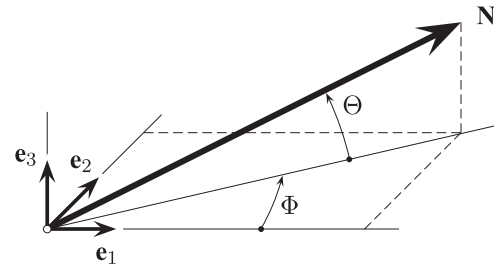
(1) are

$$\Psi_{\text{g}}(\mathbf{C}) = \frac{c}{2}(I_1 - 3), \quad \Psi_{\text{fi}} = \frac{k_1}{2k_2}[\exp(k_2 E_i^2) - 1], \quad i = 4, 6, \tag{2}$$

where the parameter c is related to the stiffness of the (isotropic) ground matrix, $I_1 = \text{tr}\mathbf{C}$ is the first invariant of $\mathbf{C}$, k_1 is a parameter with dimension of stress, k_2 is a dimensionless parameter, while E_i is a Green-Lagrange strain-like quantity given by

$$E_i = \mathbf{H}_i : (\mathbf{C} - \mathbf{I}) = AI_1 + BI_i + (1 - 3A - B)I_{\text{n}} - 1, \quad i = 4, 6, \tag{3}$$

where the constants $A = 2\kappa_{\text{op}}\kappa_{\text{ip}}$ and $B = 2\kappa_{\text{op}}(1 - 2\kappa_{\text{ip}})$ depend on the out-of-plane dispersion parameter κ_{op} and in-plane dispersion parameter κ_{ip}. The invariants I_i and I_{n} are defined as

$$I_i = \mathbf{C} : (\mathbf{M}_i \otimes \mathbf{M}_i), \quad I_{\text{n}} = \mathbf{C} : (\mathbf{M}_{\text{n}} \otimes \mathbf{M}_{\text{n}}). \tag{4}$$

Here $\mathbf{M}_4$, $\mathbf{M}_6$ represent the mean directions of the two fiber families, given by

$$\mathbf{M}_4 = \cos\alpha \mathbf{e}_1 + \sin\alpha \mathbf{e}_2, \qquad \mathbf{M}_6 = \cos\alpha \mathbf{e}_1 - \sin\alpha \mathbf{e}_2, \tag{5}$$

where α is the angle that the fiber family forms with the circumferential direction, and $\mathbf{M}_{\text{n}}$ is the unit vector normal to the plane spanned by $\mathbf{M}_4$, $\mathbf{M}_6$, e.g., the radial direction $\mathbf{e}_3$, as depicted in Fig. 3.

2.3.2. Imaging data

Images were analyzed to obtain the mean fiber angle from the circumferential direction α, the in-plane dispersion parameter κ_{ip} and the out-of-plane dispersion parameter κ_{op}, according to their definitions, see Holzapfel et al. [25]. Only the images from in-plane stacks with the highest penetration depth were used to obtain α and κ_{ip}.

First, discrete angular distributions of the relative amplitudes of fibers that resemble fiber orientations were extracted from the images by combining Fourier power spectrum analysis and wedge filtering, similar to Schriefl et al. [29,31], with a wedge width of

$5°$. Next, using the extracted data, the images were classified as isotropic or anisotropic with a R^2_{im} threshold of 0.998 [29] according to the visible fiber morphology. In the isotropic case, the concentration parameter was assigned a value of 0, i.e. $a = 0$ or $b = 0$, and no value was assigned to the fiber peak location [32]. When classified as anisotropic, the associated fiber peak positions and concentration parameters were obtained by fitting the data to $\rho_{ip}(\Phi)$ with maximum likelihood estimation for in-plane images and at $\rho_{op}(\Theta)$ using the least-squares method for the out-of-plane images. Finally, the mean fiber angle α was calculated from the standard deviation of all peak positions in the z-stack where $0°$ and $90°$ indicate the circumferential and longitudinal directions, respectively. The dispersion parameters κ_{ip} and κ_{op} were calculated using the mean concentration parameters a and b according to

$$\kappa_{ip} = \frac{1}{2} - \frac{I_1(a)}{2I_0(a)}, \quad \text{and} \quad \kappa_{op} = \frac{1}{2} - \frac{1}{8b} + \frac{1}{4}\sqrt{\frac{2}{\pi b}}\frac{\exp(-2b)}{\mathrm{erf}(\sqrt{2b})}, \tag{6}$$

where $I_1(a)$ is the modified Bessel function of the first kind of order 1, $I_0(a)$ is the modified Bessel function of the first kind of order 0, and erf is the error function defined as

$$\mathrm{erf}(x) = \frac{2}{\sqrt{\pi}}\int_0^x \exp(-\xi^2)\mathrm{d}\xi. \tag{7}$$

Note the ranges $0 \leq \kappa_{ip} \leq 1$ and $0 \leq \kappa_{op} \leq 1/2$ for the dispersion parameters. In their respective planes, $\kappa_{ip} = 0$ and $\kappa_{op} = 1/2$ correspond to perfect in-plane alignment, while $\kappa_{ip} = 1/2$ and $\kappa_{op} = 1/3$ correspond to an isotropic distribution.

2.3.3. Mechanical data

The focus of the analysis is on the elastic response of the aortic tissue. The experimental values of the Cauchy stress σ^{exp} were calculated from the force-stretch data, with $\sigma^{exp} = (F/A)\lambda$ assuming incompressibility, where F is the measured force, A is the cross-sectional area in the reference configuration, while λ denotes the stretch. The fitting was performed using the optimization toolbox lsqnonlin implemented in Matlab R2021a (The MathWorks, Inc., MA, USA). For each specimen, all available loading ratios from the maximum stretch level achieved during the tests were fitted simultaneously in the longitudinal and circumferential directions. When the structural data for a specimen were available, there were three fitting parameters (c, k_1, k_2), since the structural parameters (α, κ_{ip}, κ_{op}) were known from image analysis and were kept constant during the fitting procedure, leading to the objective function

$$e(c, k_1, k_2) = \sum_{i=1}^{n}[(\sigma_{11,i}^{mod} - \sigma_{11,i}^{exp})^2 + (\sigma_{22,i}^{mod} - \sigma_{22,i}^{exp})^2], \tag{8}$$

where n is the number of data points, σ_{11} and σ_{22} are the Cauchy stresses in circumferential and longitudinal directions, respectively. While σ^{exp} is obtained from the experimental data points as explained previously, the components of σ^{mod} can be obtained by differentiating the strain-energy function Ψ in (1) with respect to $\mathbf{C}$ to get the Cauchy stress tensor, i.e.

$$\sigma^{mod} = -p\mathbf{I} + 2\mathbf{F}\frac{\partial\Psi}{\partial\mathbf{C}}\mathbf{F}^T, \tag{9}$$

where p is the Lagrange multiplier enforcing the incompressibility assumption.

If no structural data were available for a specimen, there were six fitting parameters (α, κ_{ip}, κ_{op}, c, k_1, k_2) instead of three, and Eq. (10) was then minimized as

$$e(c, k_1, k_2, \alpha, \kappa_{ip}, \kappa_{op}) = \sum_{i=1}^{n}[(\sigma_{11,i}^{mod} - \sigma_{11,i}^{exp})^2 + (\sigma_{22,i}^{mod} - \sigma_{22,i}^{exp})^2], \tag{10}$$

The coefficient of determination R^2 was calculated as a measure of the goodness of fit, i.e.

$$R^2 = 1 - \frac{S_{res}}{S_{tot}}, \tag{11}$$

where S_{res} and S_{tot} are the sums of squares of the differences between the model/experiment and the mean of the model/experiment, respectively.

2.4. Statistics

Due to the small sample cohort, we did not assume a normal distribution and report the results in the text with the median (Q2) $\pm$ standard deviation, while the median (Q2), the 25th percentile (Q1) and the 75th percentile (Q3) are presented in the subsequent tables. Statistical differences between the four regions in terms of thickness, structural parameters, material parameters, Cauchy stress in the longitudinal and circumferential directions at 1.1 stretch were tested using the Kruskal-Wallis test followed by Dunn's test. A regression analysis was carried out to test possible correlations between different regions in the structural parameters and the material parameters using Spearman's rank correlation. In addition, correlations within each region between thickness and aneurysm diameter, structural parameters and aneurysm diameter, structural parameters and material parameters, material parameters and aneurysm diameter were investigated. Statistical significance is assumed for all tests when $p < 0.05$. Statistical analyses were performed with SigmaPlot software 10.0 (Systat Software Inc., Erkrath, Germany).

3. Results

The structural and material parameters of all specimens investigated are presented in Table 2. Although we aimed for 40 complete data sets (mechanical and structural data), 29 was achieved (6 minor, 8 anterior, 8 major and 7 posterior). Also for 2 specimens (ATAA-1 and ATAA-2 minor) only the structural data and for 5 specimens (ATAA-7 minor, ATAA-7 anterior, ATAA-7 major, ATAA-5 major and ATAA-5 posterior) only the mechanical data were available. The latter are indicated with an asterisk in Table 2, where both the structural and material parameters were obtained from mechanical data fitting according to Eq. (10).

3.1. Microstructure

Overall, the collagen fiber organization of 31 specimens (8 minor, 8 anterior, 8 major and 7 posterior) was investigated using SHG images. All specimens except the specimen from the major region of ATAA-4 showed a disordered structure in which certain layers could not be identified, possibly caused by pathological changes due to aneurysm growth. Figure 4 shows a representative collagen architecture for the four regions of ATAA-10. In all regions, images from the circumferential-radial cross sections show little to no adventitia and no intima. In addition, areas similar to the disruptions in the organization of lamellar units, e.g., glycosaminoglycans (GAG) pools, of varying sizes and distributions are observed in the media. All regions of this sample showed a value of κ_{op} close to 0.5, indicating good alignment of the fibers in the out-of-plane section. The dominant red tones in the intensity plots indicate a more isotropic dispersion in the circumferential-longitudinal plane through the penetration depth, with dark red and dark blue indicating the presence and absence of fibers in the corresponding direction, respectively.

Another representative collagen architecture for the four regions of ATAA-4 is illustrated in Fig. 5. In detail, the in-plane and out-of-plane arrangement of collagen fibers of the representative

Table 2

Material parameters (c, k_1, k_2) and structural parameters (α, κ_{ip}, κ_{op}) of all specimens according to the anatomical regions. An asterisk * indicates that all parameters were obtained by fitting mechanical data.

Region	Donor	c (kPa)	k_1 (kPa)	k_2 (–)	α (°)	κ_{ip} (–)	κ_{op} (–)	R^2
Minor	ATAA-1	–	–	–	41.00	0.22	0.49	–
	ATAA-2	–	–	–	38.00	0.32	0.47	–
	ATAA-3	0.00	10.32	8.77	49.00	0.44	0.47	0.86
	ATAA-4	12.01	0.38	72.26	21.00	0.25	0.49	0.97
	ATAA-6	33.26	0.00	15.00	15.00	0.42	0.47	0.96
	ATAA-7*	10.37*	184.53*	160.10*	47.14*	0.11 *	0.31 *	0.99*
	ATAA-8	41.00	6.57	53.48	38.00	0.39	0.49	1.00
	ATAA-9	9.31	4.24	2.30	31.00	0.38	0.47	0.96
	ATAA-10	26.46	1.69	9.00	3.00	0.49	0.49	0.99
Anterior	ATAA-1	29.57	8.24	12.18	38.00	0.34	0.49	0.98
	ATAA-2	36.48	0.00	0.00	26.00	0.25	0.50	0.21
	ATAA-3	14.96	0.93	10.91	19.00	0.32	0.47	0.95
	ATAA-4	0.00	13.16	65.83	51.00	0.40	0.49	0.75
	ATAA-6	0.00	27.80	0.00	70.00	0.32	0.46	0.80
	ATAA-7*	0.90*	6.48*	4.01*	25.00*	0.60*	0.49*	0.93*
	ATAA-8	14.38	9.90	10.14	19.00	0.40	0.49	1.00
	ATAA-9	0.00	8.91	2.32	37.00	0.37	0.49	0.92
	ATAA-10	24.25	3.05	8.06	42.00	0.43	0.47	0.96
Major	ATAA-1	52.78	20.70	21.55	23.00	0.28	0.49	1.00
	ATAA-2	17.80	0.00	49.33	12.00	0.30	0.49	0.78
	ATAA-3	0.00	35.21	0.02	44.00	0.37	0.49	0.63
	ATAA-4	3.78	17.79	44.39	41.00	0.31	0.48	0.77
	ATAA-5*	0.94*	29.94*	3.83*	18.00*	0.65*	0.50*	1.00*
	ATAA-6	18.45	25.09	0.00	18.00	0.23	0.46	0.86
	ATAA-7*	5.46*	1.30*	20.04*	25.00*	0.60*	0.49*	0.97*
	ATAA-8	0.00	33.91	5.42	13.00	0.46	0.48	0.91
	ATAA-9	14.11	1.37	11.71	40.00	0.40	0.48	0.96
	ATAA-10	19.83	1.36	13.36	4.00	0.45	0.48	0.97
Posterior	ATAA-1	7.26	104.69	0.00	47.00	0.35	0.48	0.85
	ATAA-2	16.42	0.00	0.00	29.00	0.36	0.45	0.91
	ATAA-4	9.79	0.20	106.72	40.00	0.22	0.49	0.70
	ATAA-5*	11.02*	25.57*	18.99*	18.00*	0.83*	0.50*	0.99*
	ATAA-6	19.00	0.00	0.00	10.00	0.33	0.42	0.15
	ATAA-8	36.48	0.90	19.68	8.00	0.23	0.49	0.99
	ATAA-9	13.90	2.82	3.51	21.00	0.40	0.48	0.90
	ATAA-10	16.77	12.49	2.95	8.00	0.48	0.47	0.98

Table 3

Median (Q2), as well as 25th percentile (Q1) and 75th percentile (Q3) of the structural parameters (α, κ_{ip}, κ_{op}) for minor, anterior, major and posterior regions of ATAA samples determined from SHG images.

Region	n	α (°)			κ_{ip} (–)			κ_{op} (–)		
		Q2	Q1	Q3	Q2	Q1	Q3	Q2	Q1	Q3
Minor	8	34.50	19.50	38.75	0.39	0.30	0.43	0.48	0.47	0.49
Anterior	8	37.50	24.25	44.25	0.36	0.32	0.40	0.49	0.47	0.49
Major	8	20.50	12.75	40.25	0.34	0.30	0.41	0.48	0.48	0.49
Posterior	7	21.00	9	34.50	0.35	0.28	0.38	0.48	0.46	0.49

ATAA-4 major is shown in Fig. 5(a)–(d) and (e), respectively. This sample showed highly aligned fibers in the inner media (a), with two fiber families oriented longitudinally in the inner adventitia (b), and wavy and thicker fiber bundles oriented primarily longitudinally but also circumferentially in the outer adventitia (c), see also Fig. 5(d).

Table 3 and Fig. 6 summarize the structural parameters for the four regions. The mean collagen fiber angle α from the circumferential direction among the regions was smallest in the major region ($20.50° \pm 15.33°$), followed by the posterior ($21.00° \pm 15.93°$), minor ($34.50° \pm 15.33°$), and anterior ($37.50° \pm 17.22°$) regions. There were no statistically significant differences between the four regions, however, the mean fiber angles of the minor and anterior regions were negatively correlated ($r = -0.753$ $p = 0.0212$).

There were no significant differences in the in-plane and out-of-plane dispersion parameters between the four regions. All regions show similar median values of in-plane and out-of-plane dis-

persion: minor ($\kappa_{ip} = 0.39 \pm 0.09$ and $\kappa_{op} = 0.48 \pm 0.01$), anterior ($\kappa_{ip} = 0.36 \pm 0.06$ and $\kappa_{op} = 0.49 \pm 0.01$), major ($\kappa_{ip} = 0.34 \pm 0.08$ and $\kappa_{op} = 0.48 \pm 0.01$) and posterior ($\kappa_{ip} = 0.35 \pm 0.09$ and $\kappa_{op} = 0.48 \pm 0.03$). Neither κ_{ip} nor κ_{op} were correlated between different regions.

Total wall thickness analysis for ATAA samples returned 2.67 ± 0.30, 2.10 ± 0.33, 2.20 ± 0.11 and 2.28 ± 0.43 for minor, anterior, major, and posterior regions, respectively. No significant thickness differences were observed between regions. The regression analysis did not reveal any significant correlations between the ATAA structural parameters and the aortic diameters in any of the four regions. However, aneurysm diameter correlated negatively with the wall thickness in the major region ($r = -0.663$, $p = 0.0332$).

3.2. Mechanics

A total of 34 specimens (7 minor, 9 anterior, 10 major, 8 posterior) were biaxially tested. The force-displacement response for
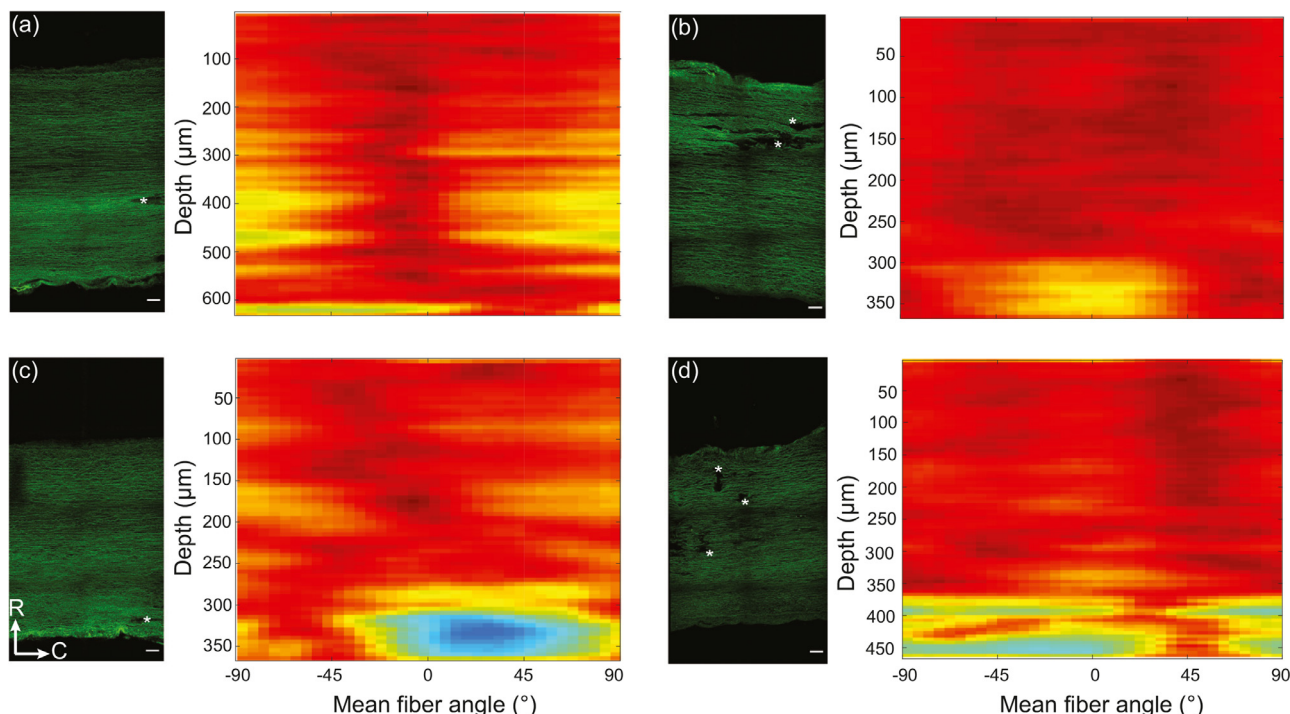
Fig. 4. Organization of collagen fibers in (a) the minor, (b) anterior, (c) major and (d) posterior regions of ATAA-10. SHG images from the radial-circumferential cross section show the disruptions in the lamellar structure and the three layers of the wall could not be identified. Scale bars equal 100 µm. Intensity plots show the orientation and dispersion of collagen fibers in the circumferential-longitudinal plane through the penetration depth. Dark red and dark blue colors indicate the presence and absence of collagen fibers, respectively. 0° corresponds to the circumferential direction. Stars indicate areas resembling local fragmentation of elastic fibers, extending to multiple lamellae. (For interpretation of the references to color in this figure legend, the reader is referred to the web version of this article.)

Table 4
Median (Q2), as well as 25th percentile (Q1) and 75th percentile (Q3) of the material parameters (c, k_1, k_2) and the associated coefficients of determination R^2 for minor, anterior, major and posterior regions of ATAA samples determined by fitting the multi-ratio planar biaxial test data.

Region	n	c (kPa)			c (kPa)			k_1 (kPa)			R^2		
		Q2	Q1	Q3	Q2	Q1	Q3	Q2	Q1	Q3	Q2	Q1	Q3
Minor	7	12.01	9.84	29.86	4.24	1.04	8.44	9.00	5.53	62.87	0.97	0.96	0.99
Anterior	9	14.38	0.00	24.25	8.24	3.05	9.90	8.06	2.32	10.91	0.93	0.80	0.96
Major	10	9.78	1.65	18.29	19.24	1.36	28.73	12.54	4.22	21.17	0.94	0.80	0.97
Posterior	8	15.16	10.71	17.33	1.86	0.15	17.76	3.23	0.00	19.16	0.90	0.82	0.98

each loading ratio became repeatable after the first 2-4 preconditioning cycles. Cauchy stress-stretch data of all specimens under equibiaxial loading at the highest available stretch level (up to 1.20), are presented in Fig. 7. Several specimens lacked pronounced nonlinearity and anisotropy. In addition, the structural parameters α and κ_{ip} from SHG image analysis, presented in Table 2, agreed well with the observations from the mechanical data regarding the anisotropy for most specimens.

More specifically, in the minor region, ATAA-3 was the only specimen showing some degree of anisotropy, while 6 others exhibited isotropy, see Fig. 7(a). In the anterior region, Fig. 7(b), ATAA-4 was the only one with marked anisotropy and nonlinearity, but the axial direction was stiffer than the circumferential direction, which is supported by the arrangement of the collagen fibers, see also Table 2. In the major region, ATAA-1, ATAA-4 and ATAA-8 showed some degree of nonlinearity and anisotropy, with the circumferential direction being stiffer, see Fig. 7(c). Finally, in the posterior region depicted in Fig. 7(d), ATAA-2 and ATAA-9 were linear and isotropic, while ATAA-1 was anisotropic and stiff but linear.

The adopted constitutive model [25] was able to provide good fits for all samples, as shown by the R^2 values in Table 4 (minor: 0.97 ± 0.05; anterior: 0.93 ± 0.25; major: 0.94 ± 0.12; posterior: 0.90 ± 0.28). Median, first (Q1) and third quartiles (Q3) of the material parameters (c, k_1, k_2) for the minor, anterior, major and posterior regions of ATAA samples, determined from the mechanical data fits, are provided in Table 4.

The Kruskal-Wallis analysis revealed no significant differences between the four regions in the median values of the material parameters: c (minor: 12.01 ± 14.89 kPa; anterior: 14.38 ± 14.19 kPa; major: 9.78 ± 16.01 kPa; posterior: 15.16 ± 9.04 kPa); k_2 (minor: 9.00 ± 58.47; anterior: 8.06 ± 20.50; major: 12.54 ± 17.48; posterior: 3.23 ± 36.40); k_1 (minor: 4.24 ± 68.38 kPa; anterior: 8.24 ± 8.36 kPa; major: 19.24 ± 14.48 kPa; posterior: 1.86 ± 36.04 kPa). The parameters c and k_1 were not correlated between regions. However, the parameter k_2, which reflects the exponential stiffening of the loading curve caused by the collagen fibers, was positively correlated between minor and major regions with a coefficient of correlation of $r = 0.786$ and $p = 0.0251$.

Potential correlations between material and structural parameters as well as between material parameters and patient data were investigated. The parameter c, related to the ground matrix, showed a negative correlation with the mean fiber angle for the posterior region with a correlation coefficient of $r = -0.901$ ($p \leq 0.001$) and parameter k_2 showed a positive correlation with κ_{op} with $r = 0.878$ ($p = 0.033$) for the minor region. The regression analysis did not reveal any significant correlations between the ATAA material parameters and the aortic diameters in any of the four regions.
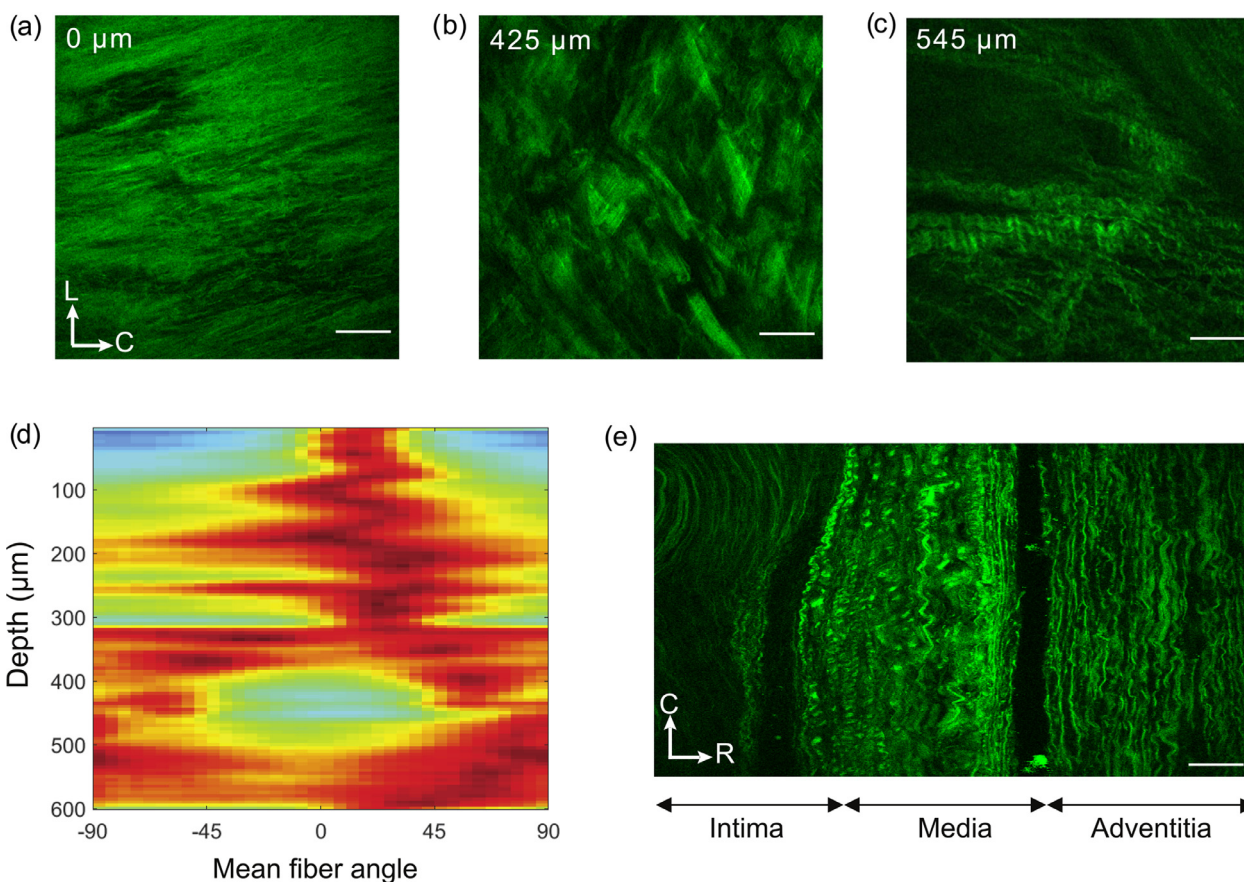
Fig. 5. Collagen fiber organization in ATAA-4 major: (a)–(c) SHG images show in-plane sections at different imaging depths; (d) intensity plot shows collagen fiber orientation and dispersion through the penetration depth, while (e) displays an image through-the-thickness. In (d), the colors range from dark blue (0%) to dark red (100%) and correspond to the relative amplitudes of the angles displayed on the x-axis. Red areas show the orientations of preferred fiber directions, while blue regions represent orientations with low fiber density. Scale bars in (a)–(c) and (e) correspond to 100 µm. (For interpretation of the references to color in this figure legend, the reader is referred to the web version of this article.)
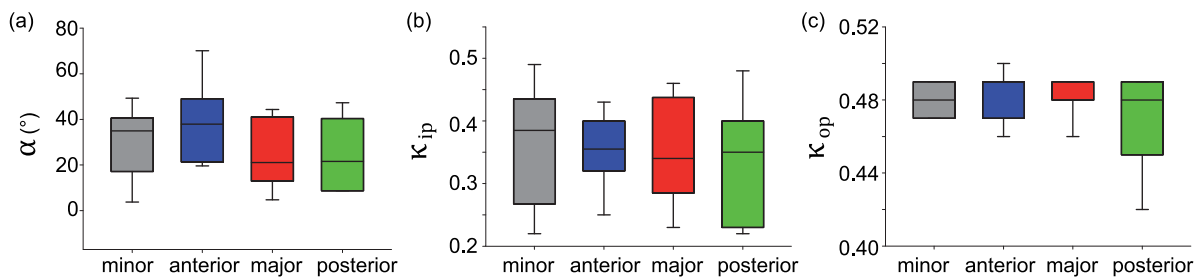

Fig. 6. Box and whisker plots of structural parameters for minor, anterior, major, and posterior regions of ATAA: (a) mean fiber angle α, (b) in-plane dispersion parameter κ_{ip}, and (c) out-of-plane dispersion parameter κ_{op}.

For quantitative comparisons, the Cauchy stress at a stretch of 1.1 under equibiaxial load was used. There were no significant differences between the regions in the circumferential direction (anterior: 9.17 ± 11.60; minor: 12.66 ± 8.16; posterior: 14.15 ± 9.68; major:16.37 ± 18.43) or in the longitudinal direction (minor: 10.37 ± 7.77; anterior:13.83 ± 30.79; major: 13.68 ± 12.65; posterior: 15.36 ± 20.74), see Fig. 8. We found a positive correlation with the major and posterior regions $r = 0.857$ and $p \leq 0.001$ in the longitudinal direction.

4. Discussion

This study aimed to demonstrate the influence of aortic tissue microstructural features on region-specific mechanics using data from multi-photon microscopy and planar biaxial extension tests.

This was investigated using the non-symmetric dispersion model, which considers a strain-energy function that includes both the mechanical and structural properties of the material proposed by Holzapfel et al. [25]. The model provided good fits for the ATAA samples despite the low number of model parameters involved. We have provided specific ranges for both structural (Table 3) and material parameters (Table 4) and for each specimen (Table 2), that could be used to develop finite element (FE) predictions of ATAA wall stress for a better understanding of the biomechanics of ATAA failure. The results underscored the importance of combining structural and mechanical analyses in investigating the region-specific differences in ATAA tissues to better understand the pathological impact on the biomechanical properties of the aorta. To our knowledge, this is the first study to investigate region-specific differences in pathological human ascending aortic tissues using
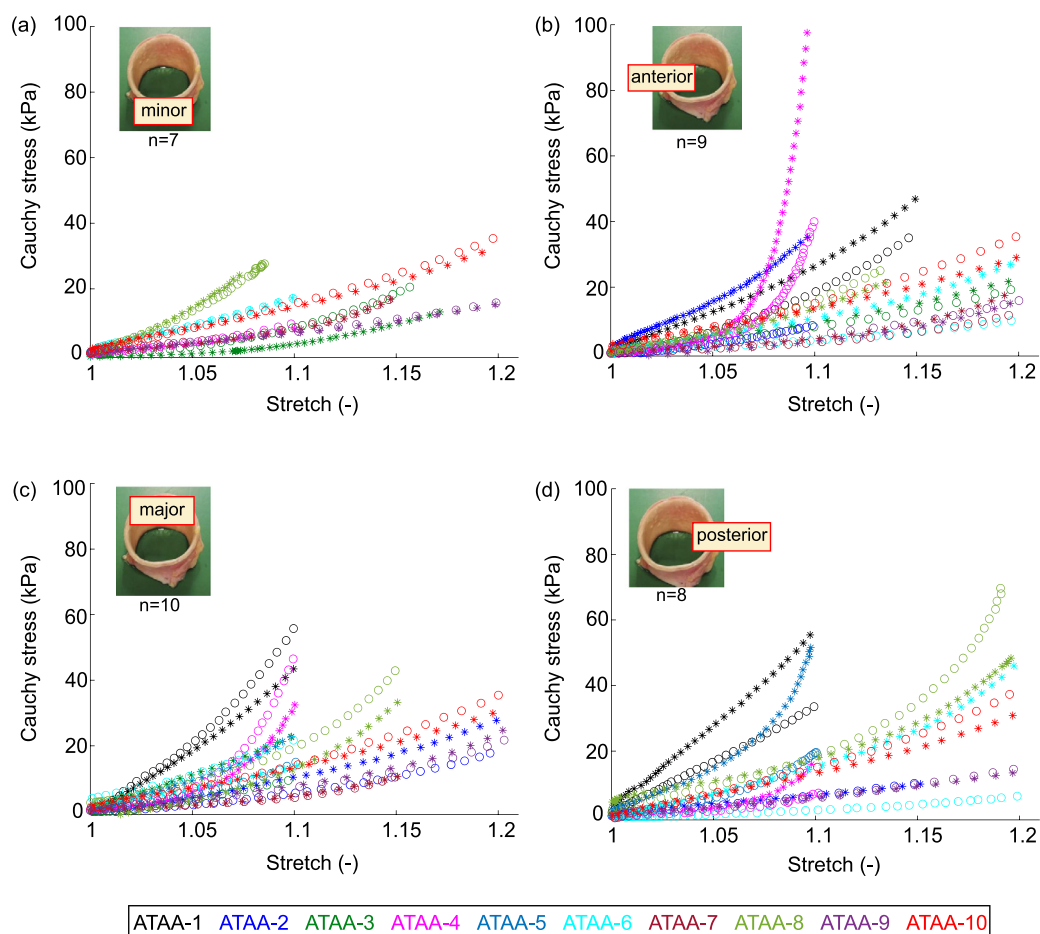
Fig. 7. Cauchy stress-stretch behavior of 10 ATAA samples obtained from equibiaxial tests, indicating substantial variability in the mechanical response: (a) minor, (b) anterior, (c) major and (d) posterior regions. Curves with open circles and asterisks correspond to the circumferential and longitudinal directions, respectively.
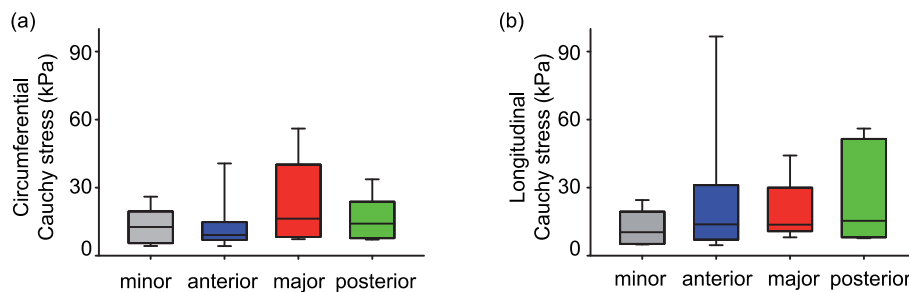

Fig. 8. Biomechanical differences between regions: Cauchy stress in (a) the circumferential and (b) the longitudinal directions at 1.1 stretch.

multi-ratio biaxial extension testing and collagen fiber organization.

4.1. Microstructure

Region-specific analyses of collagen fiber organization in aneurysmal human ascending aortas were performed in the unloaded configuration using SHG microscopy. This method enables obtaining a three-dimensional dispersion of collagen fiber orientations over the entire penetration depth, which can be increased to the entire wall thickness by optical clearing. The structural parameters describing the collagen fiber architecture, α, κ_{ip} and κ_{op}, were not found to be statistically significant between different regions. The mean fiber angle α in the major and posterior regions was closer to the circumferential direction compared with the minor and anterior regions. We found a negative correlation between the mean fiber angle of the minor and anterior regions ($p = 0.0212$). However, we advise caution as the results regarding the parameters α and κ_{ip} could be affected by the limited depth of penetration we encountered.

Qualitatively, ATAA walls showed a substantial variation in collagen architecture, with three different layers being indistinguishable. This observation is consistent with the study by Poullis [33] showing a complete loss of normal architecture and the distinction between medial and adventitial collagen organization. In addition, we observed areas that are similar to local fragmentation of elastic fibers extending into multiple lamellae as depicted in Fig. 4, which is consistent with the frequently observed GAG pools in ATAAs and aortic dissections, see, e.g., [34,35] and the references contained therein.

4.2. Mechanics

In this study, 18 ATAA specimens of 34 exhibited an anisotropic mechanical response to varying degree under biaxial loading (minor: 1/7; anterior: 8/9; major: 3/10; posterior: 6/8), but 16 specimens were isotropic. Using uniaxial tests in the circumferential and longitudinal directions, Ferrara et al. [36] reported significant anisotropy of ATAAs, with the circumferential direction being stiffer. Similar findings from uniaxial tests were reported by Iliopoulos et al. [37]. Azadani et al. [38] reported nonlinear and anisotropic response of ATAAs under biaxial loading. The isotropic response of some specimens, as well as the linear response of most specimens in our study, can partially explained by the small stretch levels achieved during the experiment. Furthermore, the high in-plane dispersion of collagen fibers, as indicated in Table 2, could be another explanation for the isotropic behavior observed in some specimens.

By analyzing Cauchy stress at 1.1 stretch, we observed variations in stiffness between regions of the aorta and found no significant differences between regions. The major region exhibited higher stiffness in the circumferential direction compared to the minor and anterior regions. In the longitudinal direction, the posterior region displayed the highest stiffness, followed by the major, anterior, and minor regions, see Fig. 8. Such variations highlight the importance of considering the specific anatomical characteristics and mechanical behavior of regions of the aorta.

The findings in the literature are consistent with our results about the major region [39,40] showing greater stiffness and the minor region showing less stiffness [39,41,42] compared to other aortic locations. Also, Ferrara et al. [36] compared the anterior and posterior regions and found that the posterior region was stiffer in the circumferential direction compared to the anterior region, while the anterior region was stiffer in the longitudinal direction than the posterior region. In contrast, another study [43] reported that the right lateral region exhibited higher stiffness compared to other regions. Therein, the increased stiffness was attributed to maladaptive remodeling due to changing loading conditions, which accelerated the naturally occurring microstructural changes associated with aging. Iliopoulos et al. [37] found uniform strength and stiffness of the ATAA tissue along the circumferential direction, while the anterior region in the longitudinal direction was the weakest and least stiff part of the aneurysm. Also, at high stresses in the longitudinal direction, the major ATAA region was stiffest. No significant difference in the maximum elastic modulus was found by Azadani et al. [44] between the anterior and posterior regions of the ascending aorta. Lower stiffness values in some regions can explain the local bulging of the ATAA wall that is common in clinical practice. For example, the study [45] demonstrated that increased stiffness of the abdominal aorta is associated with decreased collagen fiber alignment in the circumferential direction, which may predispose to aneurysm formation.

4.3. Mechanics and microstructure related

We found no influence of the aneurysm diameter on the structural and material parameters. This supports previous findings suggesting that the diameter criterion alone may be not sufficient to fully understand the properties of the aneurysm and may not adequately reflect the mechanical properties of the aortic tissue [46–48]. Moreover, the structural and material parameters were compared between the four regions of the aortic tissue and no significant differences could be found. However, the results revealed a significant correlation between structural and material parameters in two regions. More specifically, c, which relates to the ground matrix, showed a negative correlation with the mean fiber angle in the posterior region ($r = -0.901$, $p \leq 0.001$), while

k_2, associated with the stiffness of the collagen fibers, showed a positive correlation with k_{op} in the minor region ($r = 0.878$, $p = 0.033$). Furthermore, we found a significant positive correlation in the material parameter k_2 between the minor and major regions ($r = 0.786$, $p = 0.0251$). It is noteworthy that the higher value of k_2 for the major curvature indicates a stiffer mechanical behavior compared to the minor region. The lack of a corresponding correlation between the α values for these regions can be partially explained by the higher median in-plane dispersion parameter κ_{ip} and its higher variation in the minor region.

Wall stress predictions were also affected by changes in fiber architecture, supporting the conclusion that the mechanics of the aneurysm depend on the underlying fiber orientation. The collagen fiber architecture differences of the investigated anatomical regions of the aortic ring may explain the diversity in local ATAA stress states. The high stiffness value observed in the major and posterior regions of the aneurysmal aorta compared to the minor and anterior regions, as depicted in Fig. 8(a)-(b) along the circumferential direction, agrees with the trend observed in the structural analysis shown in Fig. 6(a).

Interestingly, although the median α of all regions is closer to the circumferential direction, the median Cauchy stress at 1.1 stretch was higher in the longitudinal direction for the anterior and posterior regions. Although the ATAA-4 anterior sample was not considered an outlier in the statistical analyses, it is worth noting that it could have a substantial impact on the analyses due to its pronounced nonlinearity and anisotropy compared to all other samples. Although the median α in the minor region is closer to the circumferential direction (34.50°), the median κ_{ip} is the highest among the regions and the variation in the data pushes the limits for isotropy ($\kappa_{ip} = 0.5$), see Fig. 6(a) and (b), which is reflected in the stress values, see Fig. 8(a) and (b).

Haskett et al. [45] showed that increased abdominal aortic stiffness is associated with reduced circumferential alignment of collagen fibers and may predispose patients to the development of an aneurysm. Raaz et al. [49] reported that segmental stiffening precedes abdominal aortic aneurysm growth by triggering elastin degradation. It is known that aortic stiffness is not homogeneous along the circumference of the aneurysmal ascending aorta, exposing local regions of the vessel to a greater risk of complications than the others. Based on these findings, the stiffer major and posterior regions described in the present study may be more susceptible to progressive weakening that can lead to further aneurysm growth. Taken together, these data may provide a partial explanation for the reduced biomechanical strength of the aneurysmal aorta compared to the previously reported normal ascending aorta [22]. However, less stiff aortic regions are not necessarily exposed to the greatest risk of failure due to the variability of the aortic wall strength, i.e., the ability of the material to withstand a certain load [34]. Therefore, aortic strength, as an important determinant of ATAA failure, can currently only be estimated by *ex vivo* mechanical testing to failure.

4.4. Limitations

There are several limitations in this study. First, we could not fully assess the biomechanical changes due to ATAA pathology because no control tissues were available. A comparison between structural and biomechanical properties of pathological and healthy aortic tissues should also be examined to understand possible alterations in the microstructure and then in the modification of the biomechanical behavior of aortic tissues [14,38,43]. We included only patients with the tricuspid aortic valve phenotype in this study, although biomechanical differences in the pathological ascending aortas of patients with bicuspid aortic valve and tricuspid aortic valve phenotypes have been documented [50,51].

The heterogeneity of aortic tissue requires the establishment of correlations between biomechanical characteristics and microstructural constituents, which we have attempted here. Such an approach is crucial to gain a more comprehensive understanding of the underlying pathological mechanisms. While we found some microstructural features reflected the differences in the mechanical behavior of ATAAs tissues between different regions, the mechanical behavior was not always supported by the structural measurements. This could be partially explained by the limited depth of penetration during imaging, resulting in incomplete data sets. While optical clearing methods are used to increase the penetration depth, they can lead to an isotopic shrinkage or expansion depending on the method and tissue [52]. Such dimensional changes would inevitably affect the quantification of fiber waviness, but fiber orientation and dispersion remain unaffected due to their isotropic nature [29]. In addition, although not investigated here, the content percentage of constituents and the ratio between them can affect mechanical properties. For example, the study [53] demonstrated the importance of such correlations and shed light on the intricate relationship between tissue properties and structural composition. Further investigations should aim to integrate the mechanical results obtained with additional clinical, microstructural, and genetic data from ATAA donors.

Another limitation results from the different number of specimens in the study groups (minor $n = 8$, anterior $n = 8$, major $n = 8$, posterior $n = 7$ for the structural analysis and minor $n = 7$, anterior $n = 9$, major $n = 10$, posterior $n = 8$ for the biaxial test). Such data are unpaired for the limited size of the minor region to anterior and major regions and the exclusion of specimens corresponding to unsuccessful tests. More representative conclusions could be drawn by using the same number of data in four groups of regions and increasing the number of specimens in each group. In addition, the small included patient cohort limits the ability of the present study to provide meaningful correlations with respect to other patient demographics such as aneurysm diameter, age and sex.

In addition, new data suggest that changes in the viscoelastic properties, such as hysteresis, may better reflect pathological changes and correlate with failure properties [48,51,54]. Although stress relaxation tests were conducted in the testing protocol, the present manuscript focuses solely on the elastic properties of aortic tissues and their relationship to microstructural organization. Therefore, future studies should address comprehensive analyses of both the elastic and viscoelastic properties of aortic tissues.

5. Conclusion

Although a biomechanical decision criterion is far from clinical application, the results presented here not only shed more light on the biomechanics of this challenging pathology but may also lead to better patient stratification criteria for surgery through computational modeling techniques including FE analysis [55], computational fluid dynamics [22] and fluid-solid interaction [56]. These techniques have been widely used to assess ATAA biomechanics over the past decade, but the prediction accuracy of FE models depends on the constitutive model and the reliable identification of its parameters. The set of material parameters obtained from the constitutive model used in this work are valuable for computational studies that require experimental data on human tissue samples. In most FE analyses, the orientation of the fibers is not considered, which can change the stress distribution, as demonstrated in a previous study [57]. Previous FE modeling of patient-specific ATAAs was limited to isotropic, uniaxially derived constitutive relations [58–61]. Future studies on larger patient cohorts would allow the development of a large database of constitutive

descriptors and thus the estimations of material properties for potential patients through predictive statistics.

Knowledge of the biomechanical and microstructural properties of diseased tissues is necessary to investigate the mechanics of ATAA, as the dispersed orientation of vessel fibers significantly affects the mechanical response of the tissue. This study provides a unique set of mechanical and structural data for aneurysmal human aortic samples, supporting the strong influence of the microstructure on the biomechanical tissue response in biaxial tests.

Declaration of Competing Interest

The authors declare that they have no known competing financial interests or personal relationships that could have appeared to influence the work reported in this paper.

Acknowledgments

References

[1] P.A. Iazzo, Handbook of Cardiac Anatomy, Physiology, and Devices, Springer, 2009.

[2] G.A. Kuzmik, A.X. Sang, J.A. Elefteriades, Natural history of thoracic aortic aneurysms, J. Vasc. Surg. 56 (2012) 565–571.

[3] R.R.D. Martino, I. Sen, Y. Huang, T.C. Bower, G.S. Oderich, A. Pochettino, K. Greason, M. Kalra, J. Johnstone, F. Shuj, Population-based assessment of the incidence of aortic dissection, intramural hematoma, and penetrating ulcer, and its associated mortality from 1995 to 2015, Circ. Cardiovasc. Qual. Outcomes. 11 (2018) 1–21.

[4] J.D. Humphrey, Cardiovascular Solid Mechanics. Cells, Tissues, and Organs, Springer-Verlag, New York, 2002.

[5] C. Olsson, S. Thelin, E. Stahle, A. Ekbom, F. Granath, Thoracic aortic aneurysm and dissection: increasing prevalence and improved outcomes reported in a nationwide population-based study of more than 14,000 cases from 1987 to 2002, Circulation 114 (2006) 2611–2618.

[6] M.A. Coady, J.A. Rizzo, G.L. Hammond, D. Mandapati, U. Darr, G.S. Kopf, J.A. Elefteriades, What is the appropriate size criterion for resection of thoracic aortic aneurysms? J. Thorac. Cardiovasc. Surg. 113 (1997) 476–491.

[7] J.A. Elefteriades, Natural history of thoracic aortic aneurysms: indications for surgery, and surgical versus nonsurgical risks, Ann. Thorac. Surg. 74 (2002) S1877–S1880.

[8] L.A. Pape, T.T. Tsai, E.M. Isselbacher, J.K. Oh, P.T. O'Gara, A. Evangelista, R. Fattori, G. Meinhardt, S. Trimarchi, E. Bossone, T. Suzuki, J.V. Cooper, J.B. Froehlich, C.A. Nienaber, K.A. Eagle, International Registry of Acute Aortic Dissection (IRAD) Investigators, Circulation 116 (2007) 1120–1127. Aortic diameter > or = 5.5 cm is not a good predictor of type A aortic dissection: observations from the International Registry of Acute Aortic Dissection (IRAD)

[9] A.E. Davis, A.J. Lewandowski, C.J. Holloway, N.A. Ntusi, R. Banerjee, R. Nethononda, A. Pitcher, J.M. Francis, S.G. Myerson, P. Leeson, T. Donovan, S. Neubauer, O.J. Rider, Observational study of regional aortic size referenced to body size: production of a cardiovascular magnetic resonance nomogram, J. Cardiovasc. Magn. Reson. 16 (2014) 1–9.

[10] R.R. Davies, L.J. Goldstein, M.A. Coady, S.L. Tittle, J.A. Rizzo, G.S. Kopf, J.A. Elefteriades, Yearly rupture or dissection rates for thoracic aortic aneurysms: simple prediction based on size, Ann. Thorac. Surg. 73 (2002) 17–27.

[11] J.D. Humphrey, G.A. Holzapfel, Mechanics, mechanobiology, and modeling of human abdominal aorta and aneurysms, J. Biomech. 45 (2012) 805–814.

[12] E. Saliba, Y. Sia, The ascending aortic aneurysm: when to intervene? Int. J. Cardiol. Heart Vasc. 6 (2015) 91–100.

[13] R.J. Okamoto, J.E. Wagenseil, W.R. DeLong, S.J. Peterson, N.T. Kouchoukos, T.M. Sundt, Mechanical properties of dilated human ascending aorta, Ann. Biomed. Eng. 30 (2002) 624–635.

[14] D.A. Vorp, B.J. Schiro, M.P. Ehrlich, T.S. Juvonen, M.A. Ergin, B.P. Griffith, Effect of aneurysm on the tensile strength and biomechanical behavior of the ascending thoracic aorta, Ann. Thorac. Surg. 800 (2003) 1210–1214.

[15] E.M. Isselbacher, Thoracic and abdominal aortic aneurysms, Circulation 111 (2005) 816–828.

[16] C.M. García-Herrera, J.M. Atienza, F.J. Rojo, E. Claes, G.V. Guinea, D.J. Celentano, C. García-Montero, R.L. Burgos, Mechanical behaviour and rupture of normal and pathological human ascending aortic wall, Med. Biol. Eng. Comput. 50 (2012) 559–566.

[17] J.P. Vande Geest, M.S. Sacks, D.A. Vorp, The effects of aneurysm on the biaxial mechanical behavior of human abdominal aorta, J. Biomech. 39 (2006) 1324–1334.

[18] S. Pasta, J.A. Phillippi, T.G. Gleason, D.A. Vorp, Effect of aneurysm on the mechanical dissection properties of the human ascending thoracic aorta, J. Thorac. Cardiovasc. Surg. 143 (2012) 460–467.

[19] F. Cosentino, G.M. Raffa, G. Gentile, V. Agnese, D. Bellavia, M. Pilato, S. Pasta, Statistical shape analysis of ascending thoracic aortic aneurysm: Correlation between shape and biomechanical descriptors, J. Pers. Med. 10 (2020) 28.

[20] S. Pasta, V. Agnese, A. Gallo, F. Cosentino, M.D. Giuseppe, G. Gentile, G.M. Raffa, J.F. Maalouf, H.I. Michelena, D. Bellavia, P.G. Conaldi, M. Pilato, Shear stress and aortic strain associations with biomarkers of ascending thoracic aortic aneurysm, Ann. Thorac. Surg. 110 (2020) 1595–1604.

[21] T.C. Gasser, R.W. Ogden, G.A. Holzapfel, Hyperelastic modelling of arterial layers with distributed collagen fibre orientations, J. R. Soc. Interface 3 (2006) 15–35.

[22] S. Pasta, J.A. Phillippi, T.G. Gleason, D.A. Vorp, Effect of aneurysm on the mechanical dissection properties of the human ascending thoracic aorta, J. Thorac. Cardiovasc. Surg. 143 (2012) 460–467.

[23] A. Tsamis, J.T. Krawiec, D.A. Vorp, Elastin and collagen fibre microstructure of the human aorta in ageing and disease: a review, J. R. Soc. Interface 10 (2013) 20121004.

[24] A. Tsamis, J.A. Phillippi, R.G. Koch, S. Pasta, A. D'Amore, S.C. Watkins, W.R. Wagner, T.G. Gleason, D.A. Vorp, Fiber micro-architecture in the longitudinal-radial and circumferential-radial planes of ascending thoracic aortic aneurysm media, J. Biomech. 46 (2013) 2787–2794.

[25] G.A. Holzapfel, J.A. Niestrawska, R.W. Ogden, A.J. Reinisch, A.J. Schriefl, Modelling non-symmetric collagen fibre dispersion in arterial walls, J. R. Soc. Interface 12 (2015) 20150188.

[26] G.A. Holzapfel, R.W. Ogden, S. Sherifova, On fibre dispersion modelling of soft biological tissues: a review, Proc. R. Soc. Lond. A 475 (2019) 20180336.

[27] M.R. Bersi, C. Bellini, J.D. Humphrey, S. Avril, Local variations in material and structural properties characterize murine thoracic aortic aneurysm mechanics, Biomech. Model. Mechanobiol. (2019) 203–218.

[28] G. Sommer, T.C. Gasser, P. Regitnig, M. Auer, G.A. Holzapfel, Dissection properties of the human aortic media: an experimental study, J. Biomech. Eng. 130 (2008) 021007–1–12.

[29] A.J. Schriefl, H. Wolinski, P. Regitnig, S.D. Kohlwein, G.A. Holzapfel, An automated approach for three-dimensional quantification of fibrillar structures in optically cleared soft biological tissues, J. R. Soc. Interface 10 (2013) 20120760.

[30] G. Sommer, D.C. Haspinger, M. Andrä, M. Sacherer, C. Viertler, P. Regitnig, G.A. Holzapfel, Quantification of shear deformations and corresponding stresses in the biaxially tested human myocardium, Ann. Biomed. Eng. 43 (2015) 2234–2348.

[31] A.J. Schriefl, A.J. Reinisch, S. Sankaran, D.M. Pierce, G.A. Holzapfel, Quantitative assessment of collagen fiber orientations from 2D images of soft biological tissues, J. R. Soc. Interface 9 (2012) 3081–3093.

[32] M. Jadidi, S. Sherifova, G. Sommer, A. Kamenskiy, G.A. Holzapfel, Constitutive modeling using structural information on collagen fiber direction and dispersion in human superficial femoral artery specimens of different age, Acta Biomater. 121 (2021) 461–474.

[33] M.P. Poullis, Ascending aortic curvature as an independent risk factor for type A dissection, and ascending aortic aneurysm formation: a mathematical model, Eur. J. Cardiothorac. Surg. 33 (2008) 995–1001.

[34] S. Sherifova, G.A. Holzapfel, Biomechanics of aortic wall failure with a focus on dissection and aneurysm: a review, Acta Biomater. 99 (2019) 1–17.

[35] S. Sherifova, G.A. Holzapfel, Biochemomechanics of the thoracic aorta in health and disease, Prog. Biomed. Eng. 2 (2020) 032002.

[36] A. Ferrara, S. Morganti, P. Totaro, A. Mazzola, F. Auricchio, Human dilated ascending aorta: mechanical characterization via uniaxial tensile tests, J. Mech. Behav. Biomed. Mater. 53 (2016) 257–271.

[37] D.C. Iliopoulos, R.P. Deveja, E.P. Kritharis, D. Perrea, G.D. Sionis, K. Toutouzas, C. Stefanadis, D.P. Sokolis, Regional and directional variations in the mechanical properties of ascending thoracic aortic aneurysms, Med. Eng. Phys. 31 (2009) 1–9.

[38] A.N. Azadani, S. Chitsaz, A. Mannion, A. Mookhoek, A. Wisneski, J.M. Guccione, J.M. Hope, M.D. Ge, E.E. Tseng, Biomechanical properties of human ascending thoracic aortic aneurysms, Ann. Thorac. Surg. 96 (2013) 50–58.

[39] N. Choudhury, O. Bouchot, L. Rouleau, D. Tremblay, R. Cartier, J. Butany, R. Mongrain, R.L. Leask, Local mechanical and structural properties of healthy and diseased human ascending aorta tissue, Cardiovasc. Pathol. 18 (2009) 83–91.

[40] D.C. Iliopoulos, E.P. Kritharis, A.T. Giagini, S.A. Papadodima, D.P. Sokolis, Ascending thoracic aortic aneurysms are associated with compositional remodeling and vessel stiffening but not weakening in age-matched subjects, J. Thorac. Cardiovasc. Surg. 137 (2009) 101–109.

[41] A. Duprey, K. Khanafe, M. Schlicht, S. Avril, D. Williams, R. Berguer, In vitro characterisation of physiological and maximum elastic modulus of ascending thoracic aortic aneurysms using uniaxial tensile testing, Eur. J. Vasc. Endovasc. Surg. 39 (2010) 700–707.

[42] K. Khanafer, A. Duprey, M. Zainal, M. Schlicht, D. Williams, R. Berguer, Determination of the elastic modulus of ascending thoracic aortic aneurysm at different ranges of pressure using uniaxial tensile testing, J. Thorac. Cardiovasc. Surg. 142 (2011) 682–686.

[43] T. Sigaeva, S. Sattari, S. Polzer, J.J. Appoo, E.S.D. Martino, Biomechanical properties of ascending aortic aneurysms: quantification of inter- and intra-patient variability, J. Biomech. 125 (2021) 110542.

[44] A.N. Azadani, S. Chitsaz, P. Matthews, N. Jaussaud, J. Leung, T. Tsinman, E.E. Tseng, Comparison of mechanical properties of human ascending aorta and aortic sinuses, Ann. Thorac. Surg. 93 (2012) 87–94.

[45] D. Haskett, G. Johnson, A. Zhou, U. Utzinger, J. Vande Geest, Microstructural and biomechanical alterations of the human aorta as a function of age and location, Biomech. Model. Mechanobiol. 9 (2010) 725–736.

[46] D.A. Vorp, Biomechanics of abdominal aortic aneurysm, J. Biomech. 40 (2007) 1887–1902.

[47] D.M. Pierce, T.E. Fastl, B. Rodriguez-Vila, P. Verbrugghe, I. Fourneau, G. Maleux, P. Herijgers, E.J. Gomez, G.A. Holzapfel, A method for incorporating three-dimensional residual stretches/stresses into patient-specific finite element simulations of arteries, J. Mech. Behav. Biomed. Mater. 47 (2015) 147–164.

[48] D. Eliathamby, M. Keshishi, M. Ouzounian, T.L. Forbes, K. Tan, C.A. Simmons, J. Chung, Ascending aortic geometry and its relationship to the biomechanical properties of aortic tissue, JTCVS Open 13 (2023) 32–44.

[49] U. Raaz, A.M. Zöllner, I.N. Schellinger, R. Toh, F. Nakagami, M. Brandt, F.C. Emrich, Y. Kayama, S. Eken, M. Adam, L. Maegdefessel, T. Hertel, A. Deng, A. Jagger, M. Buerke, R.L. Dalman, J.M. Spin, E. Kuhl, P.S. Tsao, Segmental aortic stiffening contributes to experimental abdominal aortic aneurysm development, Circulation (2015) 1783–1795.

[50] M. Di Giuseppe, G. Alotta, V. Agnese, D. Bellavia, G.M. Raffa, V. Vetri, M. Zingales, S. Pasta, M. Pilato, Identification of circumferential regional heterogeneity of ascending thoracic aneurysmal aorta by biaxial mechanical testing, J. Mol. Cell Cardiol. 130 (2019) 205–215.

[51] J.C.-Y. Chung, E. Wong, M. Tang, D. Eliathamby, T.L. Forbes, J. Butany, C.A. Simmons, M. Ouzounian, Biomechanics of aortic dissection: a comparison of aortas associated with bicuspid and tricuspid aortic valves, J. Am. Heart Assoc. 9 (2020) e016715.

[52] J. Xu, Y. Ma, T. Yu, D. Zhu, Quantitative assessment of optical clearing methods in various intact mouse organs, J. Biophotonics 12 (2019) e201800134.

[53] M. Nightingale, A. Gregory, T. Sigaeva, G.M. Dobson, P.W. Fedak, J.J. Appoo, E.S.D. Martino, Biomechanics in ascending aortic aneurysms correlate with tissue composition and strength, JTCVS Open 9 (2022) 1–10.

[54] M. Tang, D. Eliathamby, M. Ouzounian, C.A. Simmons, J.C.-Y. Chung, Dependency of energy loss on strain rate, strain magnitude and preload: towards development of a novel biomarker for aortic aneurysm dissection risk, J. Mech. Behav. Biomed. Mater. 124 (2021) 104736.

[55] D.P. Nathan, C. Xu, J.H. Gorman III, R.M. Fairman, J.E. Bavaria, R.C. Gorman, K.B. Chandran, B.M. Jackson, Pathogenesis of acute aortic dissection: a finite element stress analysis, Ann. Thorac. Surg. 91 (2011) 458–463.

[56] R. Campobasso, F. Condemi, M. Viallon, P. Croisille, S. Campisi, S. Avril, Evaluation of peak wall stress in an ascending thoracic aortic aneurysm using FSI simulations: effects of aortic stiffness and peripheral resistance, Cardiovasc. Eng. Technol. (2018) 707–722.

[57] S. Pasta, J.A. Phillippi, A. Tsamis, A. D'Amore, G.M. Raffa, M. Pilato, C. Scardulla, S.C. Watkins, W.R. Wagner, T.G. Gleason, D.A. Vorp, Constitutive modeling of ascending thoracic aortic aneurysms using microstructural parameters, Med. Eng. Phys. 38 (2016) 121–130.

[58] M.L. Raghavan, D.A. Vorp, M.P. Federle, M.S. Makaroun, M.W. Webster, Wall stress distribution on three-dimensionally reconstructed models of human abdominal aortic aneurysm, J. Vasc. Surg. 31 (2000) 760–769.

[59] M.F. Fillinger, M.L. Raghavan, S.P. Marra, J.L. Cronenwett, F.E. Kennedy, In vivo analysis of mechanical wall stress and abdominal aortic aneurysm rupture risk, J. Vasc. Surg. 36 (2002) 589–597.

[60] N. Wang, I.M. Tolic-Norrelykke, J. Chen, S.M. Mijailovich, J.P. Butler, J.J. Fredberg, D. Stamenović, Cell prestress. I. Stiffness and prestress are closely associated in adherent contractile cells, Am. J. Physiol. Cell Physiol. 282 (2002) C606–616.

[61] M.F. Fillinger, S.P. Marra, M.L. Raghavan, F.E. Kennedy, Prediction of rupture risk in abdominal aortic aneurysm during observation: wall stress versus diameter, J. Vasc. Surg. 37 (2003) 724–732.